Check for updates

A Novel Finite Element Model for Simulating Residual Stress in Laser Melting Deposition

Yu Zhan[1] · **Enda Zhang[1]** · **Peng Fan[1]** · **Jiateng Pan[1]** · **Changsheng Liu[2]** · **Xiangwei Kong[3]**

Abstract

The geometry of the cladding pass cross section cannot be easily predicted in laser melting deposition. Due to the huge difference between the actual and the predicted cross section, it is difficult to conduct numerical simulations. In this paper, the finite element method (FEM) with thermal–mechanical coupling is performed. A novel cladding pass cross section model, isosceles trapezoid model, is proposed. The comparisons between the isosceles trapezoid model and the traditional model (disk model and rectangle model) are performed in terms of geometrical deviation, heat dissipation, temperature field, and stress field. The results show that the geometrical deviation and heat dissipation between trapezoid model and disk model is small, and that between trapezoid model and rectangle model is large. The trapezoid model has an additional degree of freedom for modeling, i.e., contact angle, which helps to conform complex cross section geometry more flexibility. The results of temperature field and stress field show that the deviation between the isosceles trapezoid model and the traditional models is small on the upper surface of the sample, and rectangle model has worse prediction results than the other two models at the interface between cladding pass and substrate. Finally, the validation experiment is carried out and the stress is measured by laser ultrasound technique. The experimental result matches the FEM result based on isosceles trapezoid model.

Keywords FEM · Isosceles trapezoid model · Laser melting deposition · Laser ultrasound

✉ Yu Zhan
  zhanyu@mail.neu.edu.cn

  Changsheng Liu
  csliu@mail.neu.edu.cn

[1] College of Sciences, Northeastern University, Shenyang 110819, China

[2] Key Laboratory for Anisotropy and Texture of Materials Ministry of Education, Northeastern University, Shenyang 110819, China

[3] School of Mechanical Engineering and Automation, Northeastern University, Shenyang 110819, China

1 Introduction

Additive manufacturing (AM) is a relatively new fabrication process using layer manufacturing, and it was first studied in the 1970s [1]. Laser melting deposition (LMD), as a kind of most representative method of AM technology, received huge research attention. Material powder and substrate have gone through the process of melting and solidification, and along with the influence of surface tension, they form morphology in cladding pass, which results in the effect of addition in material [2, 3]. Lalas et al. [4] developed and discussed an analytical approach to the laser cladding process. The results illustrated that the formation of the cladding pass geometry is related with the solubility between cladding material and substrate material and the influence of gravity on cross section. The analytical model shows high accuracy when modeling the depth and width of the clad, but suffers from low accuracy in predicting the height. Cheikh et al. [5] observed that due to the effect of surface tension, disk cross section forms, with the size and position of the disk center dependent of technological parameters. The results indicated the good agreement between the analytical and the experimental.

FEM has been widely used to study the physics field, such as temperature fields and stress fields. Fallah et al. [6] developed a transient finite element approach to simulate the temporal evolution of the melting pool morphology and dimensions during laser powder deposition. Cladding process was simulated by activating the elements within the range of melting pool, and the prediction on geometry of cladding pass cross section was made. The simulation results were in good agreement with the experimental results. Paul et al. [7] proposed a novel fully coupled metal–thermo–mechanical model to predict residual stress and identified a critical deposition height, which was validated using neutron and X-ray diffraction measurements. The simulation result was consistent with the experimental result. Palumbo et al. [8] adopted method sequentially coupled thermal-stress analysis to simulate laser cladding in single ring pass, based on experimental data. By converting the material property within body heat source, the temperature and stress fields were obtained. 3D transient finite element model and thermomechanical analysis were performed by Zhang et al. [9] to simulate process of multi-bead laser powder deposition using arch cross sections to conform to geometry from experiment. Peyre et al. [10] adopted a three-step analytical and numerical approach to predict the geometry of manufactured structures and thermal loadings induced by the direct melting deposition process. Labudovic et al. [11] developed a three-dimensional model of laser melting powder deposition process. The results of simulation and the experimental were in good agreement. Heigel et al. [12] developed a thermo-mechanical model of directed energy deposition additive manufacturing of TC4 using measurements of the surface convection generated by gasses flowing. Three depositions with different geometries and dwell times were used to validate the model using in situ measurements of the temperature and the residual stress. Salonitis et al. [13] proposed a modeling methodology for a process chain consisting of laser cladding, as an AM process, and high speed machining. The modeling methodology was based on the finite

element method (FEM), which could predict the residual stress and part deformation. Michaleris et al. [14] investigated finite element techniques for modeling melting deposition heat transfer analyses of additive manufacturing, and the techniques for minimizing errors associated with element activation errors are proposed. Lu et al. [15] established a thermal–mechanical coupling finite element analysis model of composite lightning strike. The validity of the model was verified by comparison with the experimental results. Guo et al. [16] established a three-dimensional finite element model for calculating the residual stress based on the thermal–elastic–plastic theory, and the sequential coupling among thermal field and microstructure and mechanical properties were considered. Jiang et al. [17] proposed a fluid-thermal-solid coupling analysis method for the thermal–mechanical behavior of pressure vessel in the process of filling. Wan et al. [18] created a thermal–mechanical coupling simulation model of zirconia grinding based on the FEM to simulate the workpiece stress and the grinding temperature. The results show good agreement between the experiment and simulation. The abovementioned FEMs are based on the disk and rectangular model of cladding pass geometry. The rectangular model has high calculation efficiency, but the accuracy of stress results is low; the disk model is widely used and the stress calculation results are good, but for the calculation of complex components, the efficiency is slightly insufficient.

In this paper, a novel cross section model, isosceles trapezoid, is proposed. The comparisons between the isosceles trapezoid model and the traditional model are performed, and the results show that the accuracy deviation of the newly proposed model can be controlled reasonably. One of the remarkable advantage of isosceles trapezoid model is the contact angle, which can provide a reasonable trade-off for conforming the actual geometry of cladding pass cross section. The thermo-mechanical coupled finite element model is established and the results of temperature and stress field show that the isosceles trapezoid model and the traditional model are consistent. Then, laser ultrasound technique is used to measure the stress in Ti–6Al–4V sample produced by LMD, and the result is correlated with that obtained by FEM based on isosceles trapezoid model.

2 Building the LMD Model

LMD is a typical multi-physics coupling process, which involves the fields of mechanics, heat and optics. Here, two aspects of LMD process are studied, which are the geometry model and the heat source model. In order to simplify the model, a number of assumptions are adopted, which are flowing of the pool fluid and change of phase state of material are ignored, and melting width is assumed to be constant and the material model for TC4 is assumed to be perfectly plastic.

2.1 Geometry Model for LMD

2.1.1 Model for LMD Development in Geometry on Time Process

LMD is a dynamic process, in which the geometry changes over time as the cladding pass forms part of the workpiece. During the process, technological parameters of powder feeding rate and scanning velocity are time related, and area of the cross section of the cladding pass is determined by them. Area of the cross section of the cladding pass should be firstly obtained, as it is fundamental parameter for calculating the size of cladding pass cross section geometry. Calculation for deposition rate:

$$\dot{m}_r = \frac{m_r}{t} = \psi \dot{m}_s, \tag{1}$$

where $\dot{m}_r$ is actual deposition rate of the powder; m_r is mass of the deposited material powder; ψ is powder catchment efficiency; t is time of LMD process; $\dot{m}_s$ is powder feeding rate.

Total time of LMD process:

$$t_0 = \frac{L}{v}, \tag{2}$$

where L is total length of cladding pass; v is laser scanning velocity; t_0 is total time of DED process.

Total mass of LMD process:

$$m_0 = AL\rho = \dot{m}_r t_0, \tag{3}$$

$$A = \frac{\dot{m}_r}{v\rho} = \frac{\psi \dot{m}_s}{v\rho}, \tag{4}$$

where m_0 is total mass of LMD process; A is area of single cladding pass cross section; ρ is density of the material applied.

2.1.2 Geometry of Cladding Pass Cross Section

LMD process is accompanied by melting and re-solidification of the substrate and material powder. Under the effect of surface tension, collision from the powder and shielding gas, and cross section of the irregular forms, a certain contact angle between cladding pass and substrate is formed. In some cases, the geometry of cladding pass cross section is similar to shape disk, and for this reason some studies adopt disk model to conform to the actual results [4, 5]; In reference [9], disk cross section was adopted to conform to bead shapes in the experiment, of which contact angle and height ,respectively, are 38° and 0.28 mm. The general morphological characteristics of a single pass were introduced to demonstrate the reasonability for adopting disk model in LMD simulation. In this paper, the relatively accurate disk model and the relatively simple rectangle model are adopted as references. The comparison and analysis between disk,

rectangle and isosceles trapezoid models is performed. It is notable that actual geometry of the cladding pass is generally complex and irregular, so it is difficult to carry out accurate experimental measurement. Disk model, rectangle model and trapezoid model are all approximate models of numerical simulation, but trapezoid model proposed here has an extra degree of freedom for geometric modeling, i.e., contact angle, which can adapt to more complex modeling conditions.

Area of disk cross section:

$$A_d = \frac{1}{2}\left((2\theta)r^2 - Dr\cos\theta\right), \tag{5}$$

where A_d is the area of disk model; θ is half of the radian of the arc length of the disk cross section; r is the radius of disk; D is melting width, satisfying the relation $D = 2r\sin\theta$.

Rectangle is one of the most widely used cross section models in LMD numerical simulation to simplify geometrically modeling from the actual one in experiment. The height of rectangle can be expressed as:

$$h_r = \frac{A_r}{D}, \tag{6}$$

where h_r is the height of the rectangle.

However, there is high deviation between rectangle model and the experimental in geometry. Based on this, isosceles trapezoid cross section model is proposed, which preserves certain contact angle, and the height is the same with that of disk. Trapezoid considerably conform to the experimental, and in addition avoid the geometrical complexity of cladding pass cross section from the actual, which to some extend is better choice than rectangle, and can be a trade-off. Another advantage for trapezoid is that during geometrical modeling, after melting width and relevant technological parameter were settled, the height of rectangle and disk is determined. While for trapezoid, the one more geometrical modeling degree of freedom, contact angle, allows flexible size adjustment of the cross section, which is a superiority of trapezoid model.

The relation between parameters of trapezoid and area of cross section:

$$A_t = \frac{h_t}{2} \cdot (D + d), \tag{7}$$

$$d = D - 2h_t/\tan\alpha, \tag{8}$$

$$h_t = h_d = r(1 - \cos\theta), \tag{9}$$

where A_t is area of cross section of trapezoid; h_t is height of trapezoid; d is the length of top base; α is contact tangle of trapezoid; h_d is height of disk.

2.2 Rationality Analysis on Cross Section Models

During the numerical simulation, the one of the most basic problem is the conformity in geometry. The difference in geometry model can lead to different calculation results. Evaluation on geometrical conformity of three cross section model is performed. Outer outline functions are given below:

Disk:

$$y_d = \sqrt{r^2 - x^2} - r\cos\theta \qquad (10)$$

Rectangle:

$$y_r = h_r \qquad (11)$$

Trapezoid:

$$y_t = \begin{cases} x\tan\alpha + D/2 \,, \; x \in \left[-D/2, h_t - D/2\right) \\ h_t \,, \; x \in \left[h_t - D/2, D/2 - h_t\right) \\ -x\tan\alpha + D/2 \,, \; x \in \left[D/2 - h_t, D/2\right] \end{cases} \qquad (12)$$

2.2.1 Geometrical Deviation

In numerical simulation, there is geometrical difference in cladding pass between the models and the experimental measurement, which is due to simplification on the actual. Integration of the square of difference of the cross section outline functions, and the result of integration is used as an evaluation of geometrical conformity. Geometrical deviation index is defined as follows:

$$I_{i,j} = \int_{-\frac{D}{2}}^{\frac{D}{2}} \left(y_i - y_j\right)^2 dx, \qquad (13)$$

where $I_{i,j}$ is geometrical deviation index; y_i is the function of outer contour of cross section; i and j, respectively, refer to cross section models to be compared, with r, t and d, respectively, referring to rectangle, trapezoid and disk. According to Eq. 13, three control groups are formed between every two models.

Comparison between rectangle and disk:

$$I_{r,d} = \int_{-\frac{D}{2}}^{\frac{D}{2}} \left(y_r - y_d\right)^2 dx. \qquad (14)$$

Comparison between trapezoid and disk:

$$I_{t,d} = \int_{-\frac{D}{2}}^{\frac{D}{2}} (y_t - y_d)^2 dx. \tag{15}$$

Comparison between rectangle and trapezoid:

$$I_{r,t} = \int_{-\frac{D}{2}}^{\frac{D}{2}} (y_r - y_t)^2 dx. \tag{16}$$

In order to intuitively reflect the geometric difference between the three cross section models, relevant calculation on geometrical deviation index is performed below, seeing Sect. 4 and Table 3.

2.2.2 Heat Dissipation Evaluation

LMD process is accompanied by heat exchange between cladding pass, substrate and air. In such physics process, there is a general regularity that the larger the relative surface area, the faster the heat dissipation, in which relative surface area is the value of the ratio of surface area to volume. The calculation and comparative evaluation of relative surface area of cladding pass are performed for qualitative analysis. Since the evaluation is for cross section and also cladding pass has large aspect ratio, the calculation of relative surface area is reasonably simplified from 3-dimension to 2-dimension. As a result, the relative surface area is the value of the ratio of the perimeter to the area of cross section. Analysis is as follows.

Perimeter for closed outline of cladding pass cross section:

$$C = \int_{\Gamma} ds = \int \sqrt{1 + \left(\frac{dy}{dx}\right)^2} dx + D. \tag{17}$$

Relative surface area expression:

$$S = C/A = \frac{1}{A} \int \sqrt{1 + \left(\frac{dy}{dx}\right)^2} dx + \frac{D}{A}, \tag{18}$$

where C is perimeter for closed outline of cladding pass cross section; S is relative surface area. The comparison is performed under the same cross section area and melting width. Therefore, the evaluation process can be further simplified:

$$S' = \int \sqrt{1 + \left(\frac{dy}{dx}\right)^2} \, dx,$$

where S' is heat dissipation evaluation index. S' is equivalent to the length of the external contour of the cross section, and heat dissipation evaluation index for three cross section models are as follows:

Rectangle:

$$S'_r = 2h_r + D$$

Trapezoid:

$$S'_t = 2(\sqrt{2} - 1)h_t + D \tag{21}$$

Disk:

$$S'_d = 2r\theta \tag{22}$$

2.3 Thermal Model

2.3.1 Heat Resource Model

In this paper, double ellipsoidal power density distribution of Gaussian is adopted [19], and it is defined as follows:

$$q_f(x, y, z) = f_f \frac{6\sqrt{3}\eta P}{abc\pi^{\frac{3}{2}}} e^{-3(x^2/a_1^2 + y^2/b^2 + z^2/c^2)}, \tag{23}$$

$$q_r(x, y, z) = f_r \frac{6\sqrt{3}\eta P}{abc\pi^{\frac{3}{2}}} e^{-3(x^2/a_2^2 + y^2/b^2 + z^2/c^2)}, \tag{24}$$

where $q_f(x, y, z)$ is the front half of the quadrant of one ellipsoid heat source, and $q_r(x, y, z)$ is the rear half of the quadrant of another ellipsoid heat source; f_f and f_r are the fractions of the heat deposited in the front and rear quadrants, where $f_f + f_r = 2$; Values of $f_f = 0.6$ and $f_r = 1.4$ were good combination, which provided great correspondence between the measured and calculated thermal history results, and it is adopted in this paper; η is laser energy absorption efficiency, and the value is 0.45; P is laser power; a_1, a_2, b, c are the semi-axes of the ellipsoids, where $a_1 = a_2 = 1.5\,\text{mm}$, $b = 1.5\,\text{mm}$, $c = 0.9\,\text{mm}$. a_i is along powder feeding direction, and b is horizontally perpendicular to a_i, and c is along vertical direction. Subroutine DFLUX in ABAQUS is used to control the size and movement of heat source coded in FORTRAN. And the expressions of power density distribution considering movement are:

$$q_f(x, y, z, t) = f_f \frac{6\sqrt{3}\eta P}{abc\pi^{\frac{3}{2}}} e^{-3[(x-vt)^2/a_1^2 + y^2/b^2 + z^2/c^2]}, \tag{25}$$

$$q_r(x, y, z, t) = f_r \frac{6\sqrt{3}\eta P}{abc\pi^{\frac{3}{2}}} e^{-3[(x-vt)^2/a_2^2 + y^2/b^2 + z^2/c^2]}, \tag{26}$$

2.3.2 Surface Convection Model

The expression of surface heat loss due to convection is defined by:

$$q_L = h(\theta - \theta^0), \tag{27}$$

where q_L is surface convection; h is coefficient of convection; The surface temperature and the ambient temperature are represented by θ and θ^0. The forced surface convection model in this paper is modified from reference [12]. And the unmodified horizontal convection model adopted here is:

$$h_{\text{surface}} = 1.9(-2.717z + 37.174)e^{-(0.031r)^{1.4}} + 30, \tag{28}$$

where h_{surface} is value of convection coefficient of horizontal surface; z is the distance from the top edge of the wall to the point of interest; r is the distance from the center-line of the argon jet to the point of interest. Since it is one-layer LMD numerical simulation, appropriate simplifications are applied. Simplified model is as follows:

$$h_{\text{surface}} = 70e^{-(0.031r)^{1.4}} + 30. \tag{29}$$

The forced surface convection model is applied on upper surface of workpiece, while ignoring interfaces between active and inactive elements. During cooling process, the surfaces with forced convection go through free convection. The side surfaces and bottom of substrate go through free convection from beginning to end, with the free convection coefficient value of 10 W·m^{-2}/°C. Subroutine UFILM in ABAQUS is used to edit convection model, coded in FORTRAN.

2.3.3 Surface Radiation Model

$$q = \xi\left((\theta - \theta^Z)^4 - (\theta^0 - \theta^Z)^4\right), \tag{30}$$

where ξ is radiation constant which is equal to 0.54; θ^Z is the value of absolute zero on the temperature scale being used (Fig. 1).
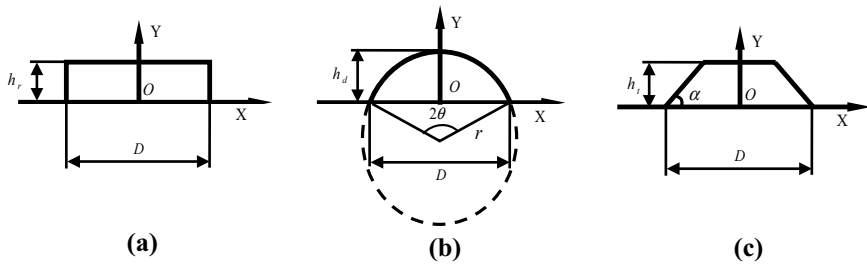
Fig. 1 Schematics of three cladding pass cross section: (a) rectangle cross section model, (b) disk cross section model, and (c) trapezoid cross section model

3 Numerical Simulation in LMD

Commercial Software ABAQUS and corresponding developed subroutines are used to simulate LMD process. The hybrid quiet/inactive element activation method is used to simulate the material deposition process. The model initially contains all the elements in the substrate, and before deposition, the elements are introduced into the set of equations. When the elements of a pass are first introduced, they are quiet, that is the material properties are scaled to be smaller so that they do not affect the analysis before they are activated. When any Gauss point of the element is consumed by the heat source volume, the properties of the element are switched from quiet to active, and the temperature of the activated element is reset to the ambient temperature. The free surface of the component is reassessed whenever an element is switch to active to ensure that radiation and convection are applied properly to the evolving part surface, including the interface between the quiet and active elements. Size of substrate is $50 \text{ mm} \times 25 \text{ mm} \times 5 \text{ mm}$, and the relative position is shown in Fig. 2. Technological parameters are displayed in Table 1.
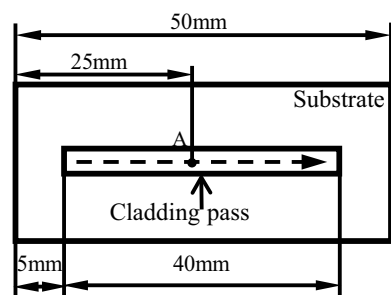
Fig. 2 Platform of cladding sample

Table 1 Process parameters of LMD in simulation and verification experiments

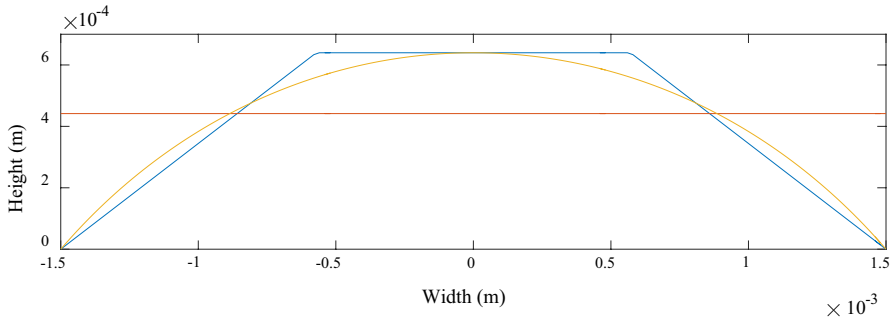| Process parameter	Value
Laser power	500 W
Scanning speed	8.5 mm·s^{-1}
Powder feeding rate	3 g·min^{-1}
Melting width	3 mm

Fig. 3 Geometry of three cladding pass cross section. The red is rectangle, the yellow is disk, and the blue is trapezoid (Color figure online)

According to analytical method in Sect. 2.1 and the parameter in Table 1, size of cladding pass cross section can be obtained, and the corresponding graphs is drawn by MATLAB shown in Fig. 3.

The material of LMD used here is Ti–6Al–4V. Density of Ti–6Al–4V is 4.44×10^3 kg m^{-3}, which is assumed to be independent of temperature. The ambient temperature is assumed to be 20 °C.

Data of material properties in Table 2 are from reference [12]. According to the assumption, change of material phase is left out, but the latent heat is still taken into account, as it is related with thermal calculation, where the value and range are, respectively, 3.65×10^5 J kg^{-1} and 1600–1670°C. Perfect plasticity is assumed in the model, which has been mentioned above. Both materials of substrate and deposition are Ti–6Al–4V. Boundary condition is that the bottom of substrate is fixed

Table 2 Temperature-dependent thermal and mechanical properties of Ti–6Al–4 V

Conductivity (W · m^{-1} · °C^{-1})	Specific heat (J · kg · °C)	Coefficient of linear expansion (°C^{-1})	Young's modulus (GPa)	Poisson ratio	Yield stress (MPa)	Temperature (°C)
6.6	565	8.64E−06	103.95	0.340	768.15	20
7.3	565	8.82E−06	100.10	0.340	735.30	93
9.1	574	9.09E−06	94.19	0.341	684.90	205
9.7	586	9.20E−06	91.81	0.345	664.65	250
10.6	603	9.33E−06	88.38	0.353	635.40	315
12.6	649	9.55E−06	82.58	0.370	585.90	425
13.9	682	9.70E−06	78.63	0.370	552.15	500
14.6	699	9.70E−06	76.52	0.378	534.15	540
17.5	770	9.70E−06	70.72	0.390	484.65	650
17.5	858	9.70E−06	64.91	0.390	435.15	760
17.5	895	9.70E−06	62.80	0.390	417.15	800
17.5	959	9.70E−06	62.80	0.390	417.15	870

and condition of symmetry is applied on symmetry plane of sample, which results in the decrease of the computation result by half. The numbers of elements in three models are 22,420 for disk, 22,020 for rectangle, and 22,020 for trapezoid. To simulate addition in cladding material, instrument of active and inactive elements is performed. Cladding pass is divided into 100 element groups along cladding direction. As the body heat source moves, elements within the heat source range are successively activated.

4 Results and Discussion

The evaluation on geometry and heat dissipation is completed by analytical method. The stress field and temperature distribution are obtained by numerical simulation, and the validation experiment about residual stress is carried out by laser ultrasound technique.

4.1 Evaluation in Geometry and Heat Dissipation

Data in Table 3 are geometric parameters and heat dissipation evaluation index of three cross section models calculated from process parameters in Table 1 based on analytical method in Sects. 2.1 and 2.2. In terms of height and contact angle of section, it is apparent that there is relatively lower conformity in rectangle model. Once the experimental geometry is fitted by the rectangular model, the deviation in geometry and heat dissipation occurs. While the geometry deviation between disk and trapezoid is the lowest and the heat dissipation difference is smallest. The Results and analysis mentioned above demonstrate that trapezoid model has relatively higher conformity in geometry and heat dissipation.

4.2 Temperature and Stress Field of Simulation

4.2.1 Temperature Field

Figure 4 presents almost the same temperature history of point A in three models. Since the heat flux conforms to Gaussian spatial distribution, in which the heat flow near the center is much stronger than that around it, in addition that point A is still in the path of the center of the heat flow, the temperature change at

Table 3 Geometry parameters and evaluation index of three cross sections

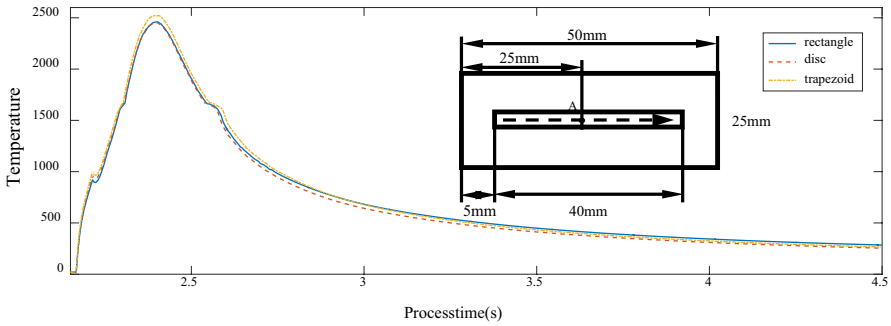| Parameter	Disk	Trapezoid	Rectangle
Height (mm)	0.6397	0.6397	0.44162
Contact angle (rad)	0.806254	0.60303	$\pi/2$
C (mm)	3.3515	3.3979	3.8832
I (mm^2)	I_{rt}=1.3572e-10	I_{rd}=1.0278e-10	I_{td}=4.3522e-12

Fig. 4 The temperature history of point A in three cross section models. Point A is located at the middle of the top

this point is mainly determined by the heat flow input intensity, and the influence from cross section morphology is very small. In Fig. 4, the temperature of point A in trapezoid is a little higher than the other two. The heat accumulated at point A after the arrival of the front edge of the heat source conducts perpendicular to the scanning direction, and for disk, the input heat is relatively less than rectangle. For trapezoid, the input heat here is between those of disk and rectangle, and in addition the trapezoidal waists limit the heat exchange, while the wider top side of rectangle provides more volume of material to conduct heat, which contributes to the highest heat accumulation in trapezoid model.

Figure 5 shows the temperature history of point B in three models. The disk and trapezoid models have similar temperature history. There is huge difference in temperature field between rectangle and the other two models. In the rectangle model, the temperature at point B begin to rise rapidly around 2.2 s, and the highest temperature reach 2000 ℃. It is because the height of rectangle is lowest in the three models, on account of which the position of point B in the heat flow is
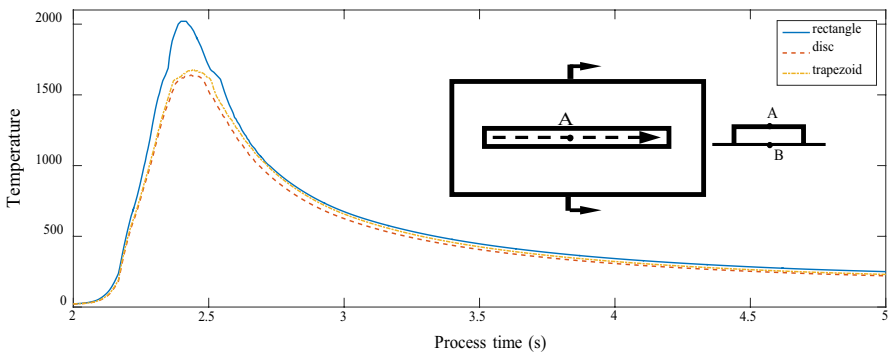

Fig. 5 The temperature history of point B in three cross section models. Point B is located at the middle of the interface between cladding pass and substrate
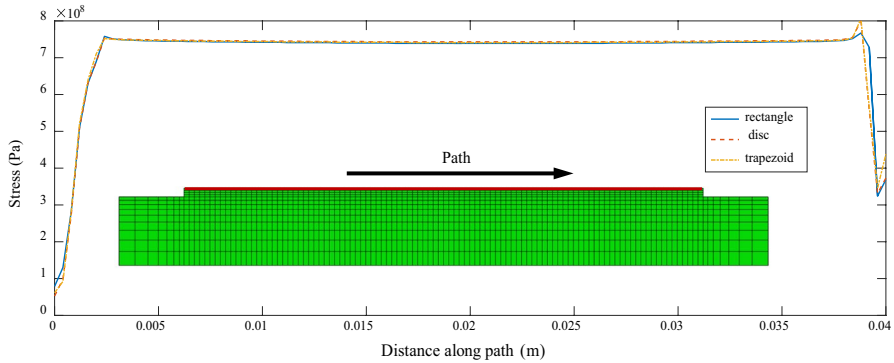
Fig. 6 The stress distribution along the path is shown in the picture, marked with a red solid line (Color figure online)
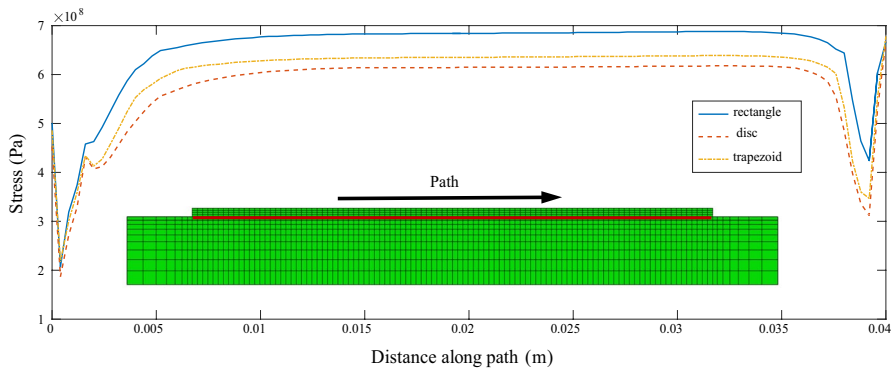

Fig. 7 The stress distribution along the path is shown in the picture, marked with a red solid line (Color figure online)

closest to the center of the body heat source in rectangle model, bringing about most intense flux and highest temperature at this point.

4.3 Stress Field

Figure 6 presents the stress distribution along the path, which consists of the nodes located at the middle of the top. As is described before, the temperature history at each node along the path is consistent, which contributes to similar stress field. The figure shows that the stress at the top of cladding pass is closed to yield limit, so it is necessary to heat treat the components made of LMD to reduce the stress.

Figure 7 shows the stress distribution along the path, which consists of the nodes located at the interface between cladding pass and substrate. For rectangle model, the stress value at each node along the path shown in the figure is close to 700 MPa, which is close to the yield limit of the material. For disk and trapezoid model, the stress value at each node along the path is around 600 MPa, fairly close to each
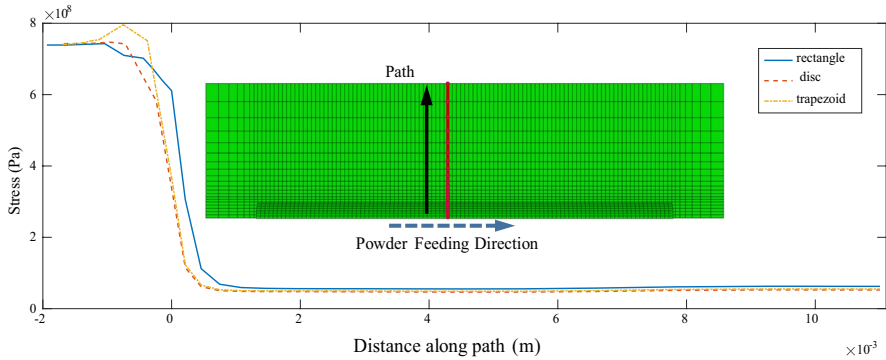
Fig. 8 The stress distribution along the path shown in the picture, marked with a red solid line (Color figure online)
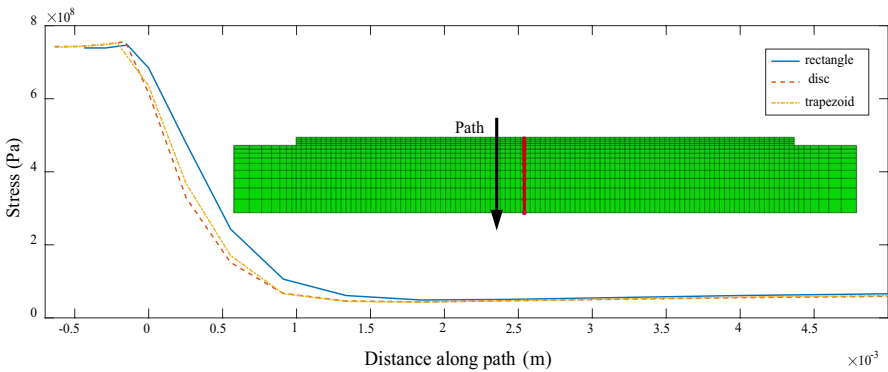

Fig. 9 The stress distribution along the path shown in the picture, marked with a red solid line (Color figure online)

other. What's more, there is a regularity can be obtained from here, that the material near the path of center of body heat source will generate relatively high stress, and the closer the material is to the path, the higher the value is.

Figure 8 shows the stress distribution along the path, which consists of the nodes located at the upper surface cladding pass and substrate. To facilitate observation, the path data are processed in a unified standard, that the point where the outer contour of cladding pass intersects the top surface of substrates is referred to as origin of abscissa, and then the right side of 0 is the stress condition of the substrate, and the left side is that of the outer contour of the three cross section models. At the right side of abscissa 0, the stress of rectangular model is significantly higher than that of the other two, resulting in a large deviation, while disk and trapezoid are consistent in this part.

Figure 9 shows the stress distribution along the path, which consists of the nodes located at the vertical center-line of cladding pass and substrate. Similarly, the path along the vertical direction is processed in a unified standard. The abscissa equal to 0 is added to the intersection point of cladding pass and the top plane of substrates.

The right side of 0 is the stress condition of the substrate along the vertical depth direction, and the left side is that of the three cross section models along the direction. Apparently, the stress of the substrate in rectangle model is higher than the other two, and this is because the depth of the body heat source in rectangle model is deeper than the other two models, which can be explained by the regularity summered above that the material near the path of center of body heat source will generate relatively high stress, and the closer the material is to the path, the higher the value is. In addition, a simple comparison of the computational efficiency of the stress field is completed. Rectangle and trapezoid models take 4 h, while disk model take 7.5 h.

4.4 Validation Experiment

The theoretical analysis and finite element calculation results show that the trapezoid model proposed in this paper has sufficient accuracy, and more degrees of freedom to be suitable for the finite element analysis of the complex component of LMD. Next, the validation experiment is carried out to further illustrate the rationality of trapezoid model. The stress in Ti–6Al–4 V sample produced by LMD is measured by laser ultrasound technique.

### 4.4.1 Basic Theory and Experimental Equipment

Laser ultrasound evaluation of the stress is based on the acoustoelastic theory, that is, the relative change in the velocity caused by stress is proportional to the latter [20]. The proportionality coefficient is called the acoustoelastic coefficient, which depends on the acoustic wave and stress direction, and also on the second- and third-order elastic constants. The first theory of surface wave in elastic material with homogeneous deformation was proposed by Hayes and Rivlin [21], and the acoustoelastic effect for ultrasound surface wave was reviewed by Pao et al. [22]. Here, only the final conclusion is provided. When the sample is in the state of uniaxial stress, and the displacement due to the propagation of surface wave is infinitesimal, then the relative variation of the propagation velocity can be expressed as:

$$\frac{\Delta v_x}{v_0} = \frac{v_x - v_0}{v_0} = K_1 \sigma_x, \tag{31}$$

where v_0 is the surface wave velocity in the material without stress; v_x is the surface wave propagation velocity along the x direction when there is stress; σ_x is the stress that needs to be measured; K_1 is the acoustoelastic coefficient of the surface wave, and it can be determined via online pre-stress loading. For Ti–6Al–4V produced by LMD, $K_1 = -9.108 \times 10^{-6}$ MPa^{-1} is calibrated in our previous research, and the experimental scheme and details of stress testing can be found in reference [23].

The laser ultrasound system is composed of ultrasound excitation module and ultrasound receiving module, as shown in Fig. 10. The Nd:YAG laser equipment (Dawa-100, Beamtech Optronics Ltd., Beijing, China) is applied to generate the ultrasound wave. Laser pulse is focused as a line source (20 mm length, 0.6 mm

Fig. 10 Laser ultrasound experimental system
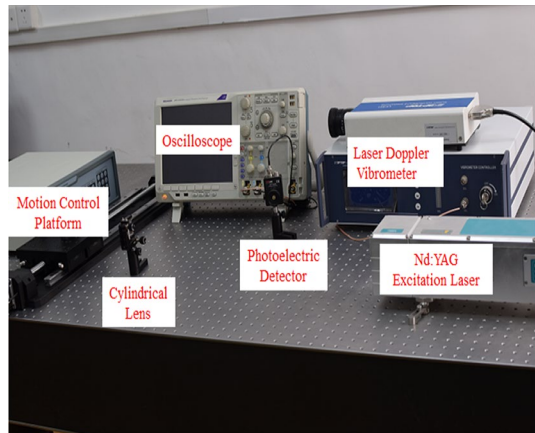
width) by the cylindrical lens to generate the surface wave. The physical parameters of the laser is pulse energy $E_0 = 100$ mJ, wavelength $\lambda = 1064$ nm, the repetition frequency $f = 20$ Hz, and pulse width $\tau = 8$ ns. The laser Doppler vibrometer (Sdptop LV-S01, Sunny Optical Technology Ltd., Suzhou, China) is applied to receive the ultrasound vibration. The He–Ne laser (frequency band 2.5 MHz, displacement resolution 0.008 nm, wavelength 632.8 nm, work distance 0.35–20 m) is sent by the vibrometer. The photoelectric detector, Thorlabs Det10A/M, with the detectable wavelength range 200–1100 nm is applied to synchronize laser shots and oscilloscope. The digital oscilloscope, Tektronix Dpo4102, with sampling rate 5 GS·s^{-1} and channel bandwidth 1 GHz, is used to store the output signals from laser Doppler vibrometer and photoelectric detector. In order to improve the signal-to-noise ratio, the signal is averaged after 64 repetitions.

4.4.2 Preparation of the Experimental Sample

The material used in LMD is Ti–6Al–4V alloy powder produced by China Aviation Melt Powder Technology Co., Ltd. The powder is spherical with a particle size of 140–200 μm. The powder has the characteristics of high sphericity, uniform composition, less than 0.1 % oxygen content and less than 2 % hollow defect. TC4 titanium alloys block prepared by traditional process are also used as the substrate. Before the experiment, the surface of the substrate is polished to remove the oxide layer and oil stain, rinsed with water and acetone, finally dried with a blower. The LMD system produced by YT Proceess Engineering Ltd is used to prepare experimental sample, as shown in Fig. 11a. The system consists of IPG fiber laser, FESZL core molding unit, Willowborg industrial machine platform and Siemens SINUMERIK CNC system. In order to compare with the simulated results, the processing parameters are set as Table 1. In the pretreatment process, the contact between air and alloy powder is minimized to avoid the oxidation of titanium in high temperature environment when printing and forming titanium alloys. Before the experiment, the LMD chamber is extracted vacuum to ensure that the oxygen in the deposition chamber is less than
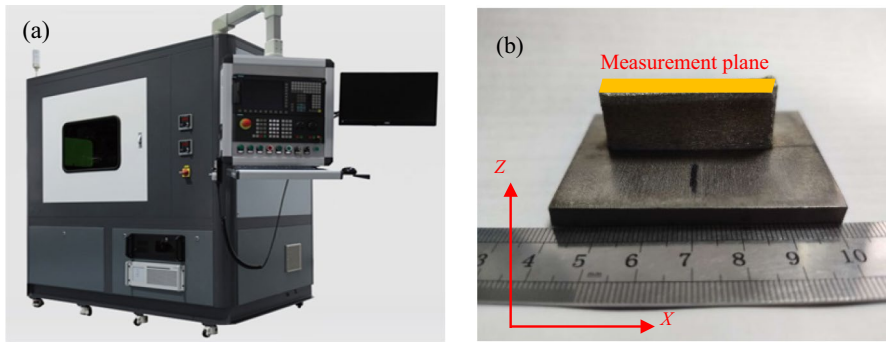
Fig. 11 Laser melting deposition system, (a) the overall appearance of the experimental system, (b) Macro size of specimens, *X* and *Z*, represent scanning and deposition directions, respectively

100 ppm. Three specimens are printed with the size of 40 mm × 15 mm × 5 mm, as shown in Fig. 11b. The stress measurement is performed on the upper surface of the specimen. The stress state and structural constraints of the surface layer are consistent with the simulated condition without considering the minor factors.

4.4.3 Comparison of Stress Result

Detailed steps and schemes for stress measurement by laser ultrasound can be found in reference [23]. Here, the final experimental results are given. Four stress measurement points are averagely arranged on the midline of the upper surface, six
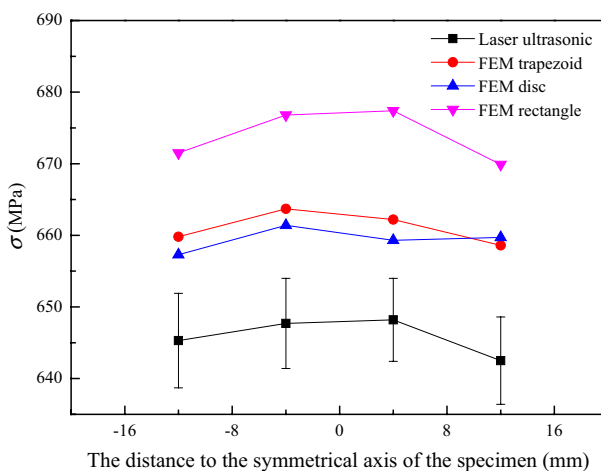

Fig. 12 The stress distribution obtained by laser ultrasound and finite element method with same process parameters

specimens are measured, and the corresponding results of each measurement point are averaged.

Figure 12 presents the residual stress distribution in the upper surface of the specimen. The error bars represent the measurement accuracy of the laser ultrasound, which is in the range of ± 10 MPa. The measurements and simulation result exhibit the same trend that the residual stress distribution near the central region of the upper surface is basically uniform, and the conclusion is consistent with the references [24]. For comparison, the simulated stress from each case is extracted from the nodes along the center-line. Due to the residual stress measured by laser ultrasound is the average stress in the range of incident depth of surface wave, the node stress in numerical results is also the average value of multiple nodes along the depth direction. The stress results of disk model and trapezoid model are very close, but the stress results of rectangle model are larger than them. The maximum stress deviation of rectangle model and trapezoid model is about 15 MPa.The error between numerical results of trapezoid model and experimental results are less than 3 %, which validate the trapezoid model proposed in this paper. Due to the limitation of computer performance, the cooling time in FEM is relatively short, which is only set to 2 min. But in the experiment, the specimen is fully cooled to prevent oxidation, cooling time is at least 10 min, large differences in cooling time may lead to errors in stress.

5 Conclusion

A novel FEM model based on the cladding pass cross section of isosceles trapezoid is proposed in this paper. The evaluation on deviation in geometry and heat dissipation of the isosceles trapezoid model and traditional model is performed. One of remarkable advantages of the isosceles trapezoid model is the one more degree of freedom in modeling, i.e., contact angle, which can satisfy the requirement of conforming complex geometry. The results of evaluation indicate that the geometrical deviation between trapezoid and disk is the smallest, and that between rectangle and disk is great. The heat dissipation deviation between rectangle and disk is the largest, and that between trapezoid and disk is the least. Then, the FEM with thermal–mechanical coupling is performed. The results of temperature and stress field show that the deviation between isosceles trapezoid model and traditional models is small on the upper surface of the sample. While the deviation between three models in the stress fields along the other paths evidently exists, which because the influence from the factor of the difference between three models in geometry is dominant. Another conclusion obtained from simulation results is that the trapezoid model can improve the computational efficiency by about 50 % compared with the disk model. Finally, laser ultrasound technique is adopted to verify the rationality of the new model. The experimental and simulated stress results are consistent. The research opens up a new path for FEM of additive manufacturing in the aspect of geometric modeling.

References

1. R. Andreotta, L. Ladani, W. Brindley, Finite element simulation of laser additive melting and solidification of Inconel 718 with experimentally tested thermal properties. Finite Elem. Anal. Des. **135**, 36–43 (2017)
2. A. Riquelme, P. Rodrigo, M.D. Escalera, J. Rams, Analysis and optimization of process parameters in Al-SiCp laser cladding. Opt. Lasers Eng. **78**, 165–173 (2016)
3. D.D. Gu, B.B. He, Finite element simulation and experimental investigation of residual stresses in selective laser melted Ti–Ni shape memory alloy. Comput. Mater. Sci. **117**, 221–232 (2016)
4. C. Lalas, K. Tsirbas, K. Salonitis, G. Chryssolouris, An analytical model of the laser clad geometry. Int. J. Adv. Manuf. Technol. **32**, 34–41 (2007)
5. H. El Cheikh, B. Courant, J.Y. Hascoët, R. Guillén, Prediction and analytical description of the single laser track geometry in direct laser fabrication from process parameters and energy balance reasoning. J. Mater. Process. Technol. **212**, 1832–1839 (2012)
6. V. Fallah, M. Alimardani, S.F. Corbin, A. Khajepour, Temporal development of melt-pool morphology and clad geometry in laser powder deposition. Comput. Mater. Sci. **50**, 2124–2134 (2011)
7. S. Paul, R. Singh, W. Yan, I. Samajdar, A. Paradowska, K. Thool, M. Reid, Critical deposition height for sustainable restoration via laser additive manufacturing. Sci. Rep. **8**, 1–8 (2018)
8. G. Palumbo, S. Pinto, L. Tricarico, Numerical finite element investigation on laser cladding treatment of ring geometries. J. Mater. Process. Technol. **155**, 1443–1450 (2004)
9. C. Zhang, L. Li, A. Deceuster, Thermomechanical analysis of multi-bead pulsed laser powder deposition of a nickel-based superalloy. J. Mater. Process. Technol. **211**, 1478–1487 (2011)
10. P. Peyre, P. Aubry, R. Fabbro, R. Neveu, A. Longuet, Analytical and numerical modelling of the direct metal deposition laser process. J. Phys. D Appl. Phys. **41**, 025403 (2008)
11. M. Labudovic, D. Hu, R. Kovacevic, A three dimensional model for direct laser metal powder deposition and rapid prototyping. J. Mater. Sci. **38**, 35–49 (2003)
12. J.C. Heigel, P. Michaleris, E.W. Reutzel, Thermo-mechanical model development and validation of directed energy deposition additive manufacturing of Ti-6Al-4V. Addit. Manuf. **5**, 9–19 (2015)
13. K. Salonitis, L. D'Alvise, B. Schoinochoritis, D. Chantzis, Additive manufacturing and post-processing simulation: laser cladding followed by high speed machining. Int. J. Adv. Manuf. Technol. **85**, 2401–2411 (2016)
14. P. Michaleris, Modeling metal deposition in heat transfer analyses of additive manufacturing processes. Finite Elem. Anal. Des. **86**, 51–60 (2014)
15. X. Lu, M.J. Luo, M. Zhao, Z.Z. Shan, Thermal coupling analysis of lightning strike laminates. J. Aeronaut. Mater.s **40**, 35–45 (2020)
16. Q.H. Guo, B.S. Du, G.X. Xu, D.G. Chen, L.C. Ma, D.F. Wang, Y.Y. Zhang, Influence of filler metal on residual stress in multi-pass repair welding of thick P91 steel pipe. Int. J. Adv. Manuf. Technol. **110**, 2977–2989 (2020)
17. Y. Jiang, S.T. Wei, P. Xu, Influences of filling process on the thermal mechanical behavior of composite overwrapped pressure vessel for hydrogen. Int. J. Hydrogen Energy **45**, 23093–23102 (2020)
18. L.L. Wan, L. Li, Z.H. Deng, W. Liu, Thermal-mechanical coupling simulation and experimental research on the grinding of zirconia ceramics. J. Manuf. Process. **47**, 41–45 (2019)
19. J. Goldak, A. Chakravarti, M. Bibby, A new finite element model for welding heat sources. Metall. Trans. B **15**, 299–305 (1984)
20. L.M. Dong, J. Li, C.Y. Ni, Z.H. Shen, X.W. Ni, Evaluation of residual stresses using laser-generated SAWs on surface of laser-welding plates. Int. J. Thermophys. **34**, 1066–1079 (2013)
21. M. Hayes, R.S. Rivlin, Surface waves in deformed elastic materials. Arch. Ration. Mech. Anal. **8**, 358–380 (1961)

22. Y. Pao, W. Sachse, H. Fukuoka, Acoustoelasticity and ultrasonic measurements of residual stresses, in *Physical Acoustics*, vol. 17, ed. by W.P. Mason, R.N. Thurston (Academic Press, New York, 1984), pp. 61–143

23. Y. Zhan, C. Liu, J.J. Zhang, G.Z. Mo, C.S. Liu, Measurement of residual stress in laser additive manufacturing TC4 titanium alloy with the laser ultrasonic technique. Mater. Sci. Eng. A **762**, 138093 (2019)

24. T. Mukherjee, W. Zhang, T. DebRoy, An improved prediction of residual stresses and distortion in additive manufacturing. Comput. Mater. Sci. **126**, 360–372 (2017)